Laser Beacon Tracking for High-Accuracy Attitude Determination

Tam Nguyen

Department of Aeronautics and Astronautics, Massachusetts Institute of Technology
77 Massachusetts Avenue, Cambridge, MA 02139; 617-710-1845
tamz@mit.edu

Faculty Advisor: Kerri Cahoy
Department of Aeronautics and Astronautics, Massachusetts Institute of Technology

ABSTRACT

CubeSat pointing capabilities have greatly improved in the past few years, paving the way for more sophisticated science and technology demonstration missions. Advances in attitude determination have led to the development of several CubeSat-sized attitude sensors capable of achieving fine attitude knowledge, most of which utilize natural light sources as references, such as in the case of star trackers and sun sensors. However, inertial-based attitude sensors often limit ground tracking capability of the satellite due to high ephemeris uncertainty of most CubeSats. Laser beacon tracking directly measures of the satellite's attitude relative to a ground station or target, eliminating attitude errors induced in the coordinate frame conversion process. In addition, the use of a narrow-band artificial light source allows filtering techniques to be implemented, reducing the probability of false positives. In this paper, we present the development of a low-cost CubeSat-sized laser beacon camera along with detailed simulation development and results to demonstrate the attitude sensing performance of the module. The end-to-end simulation includes a laser link radiometry model, hardware model, atmospheric scintillation model, and sky radiance model at the beacon wavelength. Simulation results show that the laser beacon camera is capable of achieving an attitude accuracy of less than 0.1 mrad with a fade probability of less than 1% during daytime under most sky conditions for a satellite above 20º elevation in low-Earth orbit.

BACKGROUND

Recent developments in miniaturized attitude sensors have allowed CubeSats to achieve advanced science and technology demonstration missions. Devices such as star trackers are capable of achieving sub-milliradian attitude knowledge, realized by star field imaging techniques[1]. However, accurate attitude knowledge in inertial space does not guarantee accurate pointing knowledge relative to a ground target due to ephemeris uncertainty. For example, 1-km orbit ephemeris error of a satellite at 500-km altitude leads to an error of 0.1º in attitude when converting from inertial to Earth-fixed frame. Many CubeSats do not have access to the Global Positioning System (GPS) receivers and have to rely on published Two-line Element (TLE) data for orbit determination, which could lead to orbit error of several kilometers[2]. This induced error limits CubeSats that require accurate ground target pointing from leveraging attitude sensing capability from inertial-based attitude sensors. Ground laser beacon detection is an attitude sensing architecture that allows CubeSats to directly acquire the location of a ground target and use this information for attitude determination. In addition, ground beacon can be designed to enhance detection probability, which is not a possibility when natural light sources are used as

reference. For example, the laser beacon can be designed to have a narrow-band spectrum, allowing band-pass filtering techniques to be implemented at the receive terminal to reduce background light interference, improving attitude sensing performance.

Laser beacon detection techniques have been demonstrated by laser communication missions on larger satellite platforms that require accurate ground station pointing, such as the Laser Lunar Communication Demonstration (LLCD) and the Optical Payload for Lasercom Science (OPALS). The LLCD mission demonstrated an attitude accuracy of 2.5 µrad from a lunar orbit[3]. OPALS is a laser communication module onboard the International Space Station, achieving a pointing accuracy on the order of 300 µrad [4]. Aerospace Corporation's Optical Communication and Sensor Demonstration (OCSD) will be the first CubeSat to employ laser beacon sensing technique, aiming to achieve a pointing accuracy of 0.1º [5].

This paper presents the design and performance analysis of a miniaturized laser beacon camera, consisting of only commercial off-the-shelf (COTS) components, that can achieve an attitude accuracy of less than 0.1 mrad (0.006º) with a fade probability of less than 0.3% under

clear-sky, daytime conditions and 1% under cloudy, daytime conditions at low elevation angles. The beacon tracking camera is a fine attitude sensor, designed to operate within $\pm 3^{\circ}$ pointing error relative to the ground station, which is assumed to be provided by other attitude sensors on the satellite in conjunction with the satellite's attitude actuators. We first present the system architecture, baseline requirements, and beacon camera hardware development. The next section describes a detailed simulation of the laser beacon detection process, including link radiometry, hardware model, atmospheric turbulence model, and Earth's upwelling radiance model. Finally, the simulation results are presented to assess the accuracy and reliability of the approach under various sky conditions and orbit configurations, demonstrating its applicability for CubeSat high-accuracy attitude sensing.

SYSTEM OVERVIEW

The laser beacon tracking architecture consists of a laser source, transmitted from a ground station and detected by an on-orbit camera at the satellite terminal after propagating through the atmospheric channel. An illustration of the laser beacon tracking configuration is shown in Figure 1. The ground-based laser source is launched through a telescope, which controls the beam divergence angle necessary to cover the satellite's position uncertainty. The telescope is mounted on a steering platform, allowing continuous tracking of the satellite over each ground pass. The beacon wavelength was chosen to be in the near-infrared (NIR) range to comply with eye-safety regulation while maintaining sufficient sensitivity with standard Silicon focal plane arrays, reducing cost while increasing product availability. Laser propagation through the atmosphere is a complex process, leading to both attenuation from atmospheric absorption and scattering as well as brightness fluctuations due to the turbulent nature of the atmosphere. Upwelling Earth brightness presents the main source of background radiance, varying significantly based weather conditions and time of day. At the satellite terminal, the laser beam is detected by a beacon camera, consisting of a focal plane array, lens system, and filters. The camera's field-of-view (FOV) is chosen to be sufficiently wide to compensate for coarse attitude control capability while narrow enough to reduce the amount background light in the system. Filters are used to select the spectral band of the transmit laser and to reduce the effect of ultraviolet light in the optical system. Since the beacon is effectively a point source, the beacon image follows the point-spread function (PSF) of the lens system, sampled according to the resolution of the focal plane array. Once the beacon is detected by the camera, image processing techniques such as thresholding and centroiding can be applied to find the pixel location of the beacon image on the focal plane array. This information directly correlates to the direction of the beacon relative to the spacecraft's body coordinate system, providing ground-referenced attitude knowledge for the satellite.
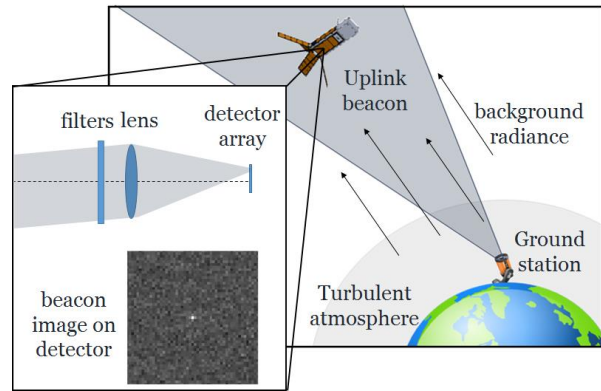
Figure 1 Laser beacon tracking architecture

LASER BEACON CAMERA DESIGN

The beacon camera design goal is to achieve sufficient beacon signal-to-noise ratio for detection while maintaining a small form factor to meet CubeSat's size and mass constraints. A secondary goal is to keep the module at a low cost, which led to the decision of using only commercial off-the-shelf (COTS) products. The system is designed to detect a laser beacon at 850 nm, a common NIR wavelength at which many laser and optical components are available. The current beacon camera prototype is shown in Figure 2. The system size is approximately 40 mm x 40 mm x 60 mm with a total weight of 120 g.

Figure 2 Laser beacon camera prototype

The beacon camera prototype consists of a focal plane array, lens system, band-pass filter, and long-pass filter. To reduce cost and expand the option pool, a standard Complementary Metal-Oxide Semiconductor (CMOS) Silicon detector array was selected. The main parameters considered during the detector selection process include array format, sensitivity, and noise properties. Through

many design iterations, the Aptina MT9P031 detector was selected because of its high resolution, high sensitivity at 850 nm, as well as low dark current and read noise properties. The lens system is an off-the-shelf product from EdmundOptics with a 1" aperture and a focal length that provides approximately 6.6° FOV with the sensor format, to compensate for expected pointing error from CubeSat coarse attitude control. Two optical filters are utilized in the system: a band-pass filter at the beacon wavelength and a long-pass filter to protect the lens system from heating and darkening due to solar radiation. Table 1 summarizes the detailed specifications of the beacon camera.

Table 1 Beacon camera specifications[6, 7]

Detector array	
Sensor format	1/2.5 in
Resolution	5 Mpixels
Pixel size	2.2 μm
Quantum efficiency (at 850 nm)	12%
Lens	
Aperture diameter	1 in
Focal length	35 mm
Filters	
Band-pass filter transmission	(850 +/- 5) nm
Long-pass filter transmission	>700 nm

SIMULATION DEVELOPMENT

An end-to-end simulation was constructed in MATLAB to generate the expected beacon image on the detector array. These images will be used to identify the expected attitude accuracy and fade probability of the system through basic image processing techniques. Figure 3 summarizes the simulation structure in a block diagram format. There are four main models constructed in the simulation: link radiometry model, receiver hardware model, atmospheric turbulence model, and Earth upwelling radiance model. The uplink beacon radiometry model is used to compute the expected optical power density at the spacecraft's receive aperture given the transmitter's properties and orbit configurations. The receiver hardware properties model provides lens and detector properties of interest such as the point-spread function (PSF), detector's resolution, and noise properties. The atmospheric turbulence model simulates the effect of refractive index inhomogeneity and dynamic wind flow in the atmosphere, causing received power fluctuations. The Earth upwelling radiance under various sky conditions was inspected to provide the expected background noise level of each frame. All four models were combined in the beacon

image generation script, creating the expected image of the beacon beam on the detector array.
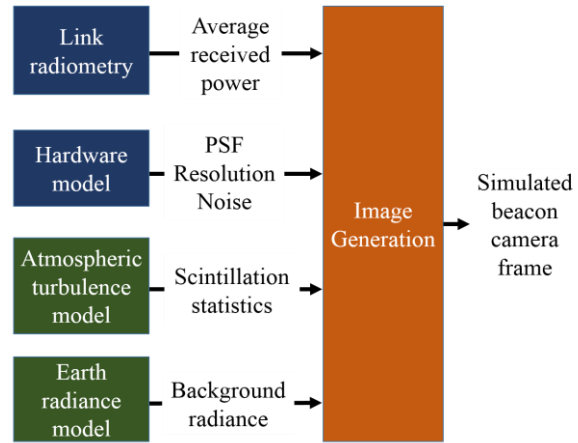
Figure 3 Beacon simulation block diagram

Link radiometry

The goal of the link radiometry analysis is to compute the average received power through the beacon camera, given the transmitter properties, channel parameters, and receive aperture. An illustration of the link configuration along with relevant parameters are shown in Figure 4.
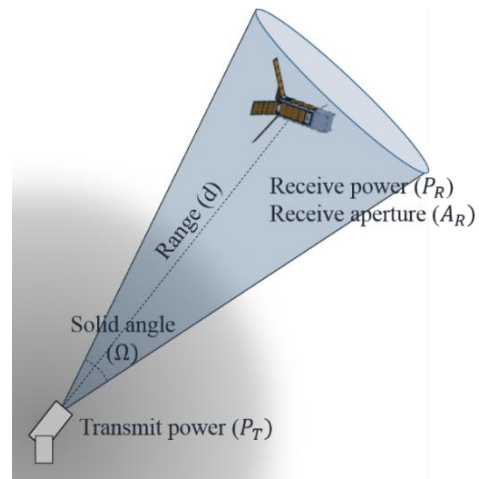
Figure 4 Link radiometry configuration

The transmit laser power and beam solid angle are critical parameters in the transmitter design. The transmit power available is limited by cost and commercial availability of laser diodes and drivers as well as aviation eye-safe limit from the Federal Aviation Administration (FAA)[8]. The laser beam is assumed to have uniform intensity within the beam solid angle, an adequate assumption for the average power analysis. The beacon beamwidth is sized to accommodate the tracking error of the transmit laser steering mount during beacon acquisition. For example, an ephemeris error of 1 km of

a satellite at 400 km altitude at zenith will lead to a full-angle beacon beam divergence of approximately 5 mrad. The channel losses considered in this analysis includes free-space path loss, atmospheric absorption and scattering, and optics loss. Free-space path loss increases as the square of the satellite-to-ground range, which can be in the order of 1000 km for a satellite in low-Earth orbit (LEO) at low elevation angle. Atmospheric absorption and scattering loss is a function of wavelength and have been commonly estimated using the MODerate resolution atmospheric TRANsmission (MODTRAN) model. The attenuation level at 850 nm is expected to be on the order of -4 dB to -6 dB for an Earth-space link at low elevation angle[9]. Optics losses on both transmit and receive platforms can be estimated using commercial telescope and camera performances. The link radiometry calculation with transmitter, receiver, and channel parameters can be simplified as shown in Equation 1, where P_R, P_T are the transmit and receive power, respectively, A_R represents the receive aperture's area, Ω is the beam solid angle, d is the ground-to-satellite range, L_A, L_o are the atmospheric and optics loss, respectively.

$$P_R = P_T \frac{4\pi}{\Omega} \cdot \frac{1}{4\pi d^2} \cdot \frac{1}{L_A} \cdot \frac{1}{L_O} \cdot A_R \qquad (1)$$

Table 2 presents a sample link radiometry result for a 10-W laser transmitter to a satellite in a 400 km orbit at 20° elevation, with estimated atmospheric losses and hardware properties. The average photon rate received by the detector can be found from the average received power and photon energy at the beacon wavelength.

Table 2 Sample link radiometry analysis[7, 9]
(10-W laser, 400 km altitude, 20° elevation)

Transmitter properties		
Average laser power	10	W
Uplink wavelength	850	nm
Beam divergence	5	mrad
Free-space/Atmospheric channel		
Range	984	km
Atmospheric absorption/scattering	-5	dB
Receiver properties		
Receiver bandwidth	10	nm
Average power at detector	0.013	nW
Average photon rate	5.7×10^7	photons/s

Receive hardware model

The optical power received by the aperture is distributed in a point-spread function (PSF) on the focal plane array with size, shape, and resolution defined by the camera hardware properties. The beacon camera components were modeled based on manufacturers' specifications and preliminary hardware testing. The lens system's Zemax model was provided by the vendor, allowing the lens response to be analyzed for a variety of field angles. Figure 5 shows the normalized PSFs of the on-axis and off-axis case, respectively, produced by the Zemax model, along with the diffraction limit circle, for scaling purpose.
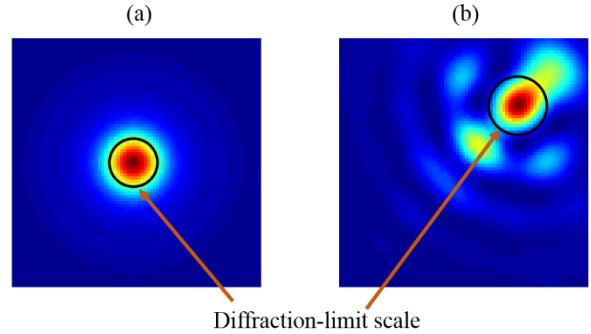
Figure 5 (a) On-axis PSF (b) Off-axis PSF ($\theta_x = 3.3°$, $\theta_y = 3.3°$)

The PSF images are sampled according to the detector's resolution, as shown in Figure 6 (a.1) and (b.1). The brightest pixel flux fraction (BPFF) parameter was used as a figure of merit in each case. The images cross sections are shown in Figure 6 (a.2) and (b.2), along with the corresponding BPFF for the on-axis and off-axis case. While aberrations exist in the off-axis case causing PSF distortions, the off-axis BPFF stays relatively close to the on-axis case. Since the BPFF will determine the signal-to-noise ratio of the system and detection probability, the on-axis PSF will be used in the simulation as a first-order approximation.

The optical power on the detector was converted to a number of electrons based on the photon power at the wavelength of interest and the detector's quantum efficiency. The charge on each pixel was further adjusted to include detector's noise parameters. Read noise was modeled as a Gaussian random parameter with the root-mean square value provided in the detector's data sheet. Dark current noise was modeled as a Poisson distribution with the mean at the average dark current value provided by the manufacturer. Multiple dark frames were taken with the camera prototype to investigate the number of bright damaged pixels. The result shows that there are less than 10 permanently bright pixels with the brightest pixel at 0.8% well capacity. The effect of these damaged pixels was incorporated in the simulation by randomly selecting a number of pixels and setting their values to the expected brightness.

(a.1)   (b.1)

(a.2)   (b.2)

BPFF = 0.120   BPFF = 0.114
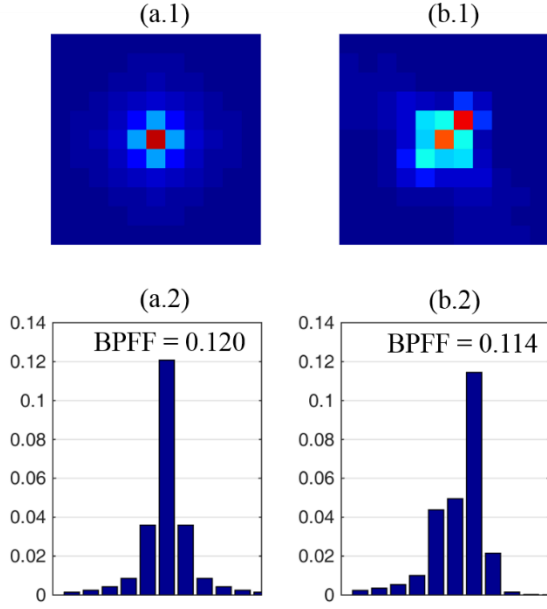
Figure 6 (a.1) On-axis PSF as sampled by the detector (a.2) Normalized pixel value of the cross section with the brightest pixel (on-axis) (b.1) Off-axis PSF as sampled by the detector (b.2) Normalized pixel value of the cross section with the brightest pixel (off-axis)

Atmospheric turbulence model

The uplink beacon propagates through Earth's turbulent and inhomogeneous atmosphere, causing random irradiance fluctuations at the receiver's end, referred to as scintillation. The effect of scintillation on the uplink path is more drastic than the downlink path due to the beam being distorted early on its path in the atmosphere before propagating in free space. For this reason, the satellite aperture always lies within the same atmospheric coherence zone, causing the entire received image to fade or surge corresponding to the turbulence dynamic[10]. Scintillation depends greatly on the atmospheric turbulence strength, which can be quantified by the refractive index structure parameter (C_n^2). C_n^2 varies according to several parameters such as geographical location, weather conditions, and time of day. One of the most commonly used C_n^2 parametric models for daytime conditions is the Hufnagel-Valley model, shown in Equation 2.[11,12]

$$C_n^2(h) = 0.00594 \left(\frac{w}{27}\right)^2 \left(10^{-5}\,h\right)^{10} e^{(-h/1000)} + 2.7 \times 10^{-16} e^{(-h/1500)} + A e^{(-h/100)} \tag{2}$$

where h represents altitude measured in m, w is the root-mean-square (rms) windspeed in m/s, and A is the nominal value of $C_n^2(0)$ at ground level in $m^{-2/3}$. The rms wind speed w can be found as a function of the ground wind speed V_g and slew rate ω_s, as shown in Equation 3a and 3b.[11] For a satellite in LEO moving with respect to an observer on the ground, the corresponding slew rate can get up to 1°/s, a dominant contribution to the wind speed value at high altitude.

$$w = \left[\frac{1}{15 \times 10^3} \int_{5\times10^3}^{20\times10^3} V^2(h)\,dh\right]^{1/2} \tag{3a}$$

$$V(h) = \omega_s h + V_g + 30 \exp\left[-\left(\frac{h-9400}{4800}\right)^2\right] \tag{3b}$$

With the C_n^2 profile of the atmosphere, the scintillation index of a laser beam along the uplink channel can be determined following the strong fluctuation theory. The scintillation index σ_I^2 can be derived as shown in Equation $4a - 4c$, where H is the satellite altitude, k is the wavenumber of the beam, and ζ is the off-zenith angle.[11] To reduce the effect of scintillation, spatial diversity is often used where multiple transmit lasers are mounted in different coherence zones. Since each beam propagation process can be treated as statistically independent, the scintillation index can be scaled down with the number of independent beams.

$$\sigma_I^2 = \exp\left[\frac{0.49\,\sigma_{Bu}^2}{\left((1 + 1.12\,\sigma_{Bu}^{12/5}\right)^{7/6}} + \frac{0.51\,\sigma_{Bu}^2}{\left(1 + 0.69\sigma_{Bu}^{12/5}\right)^{5/6}}\right] - 1 \tag{4a}$$

$$\sigma_{Bu}^2 = 8.70\,\mu_{3u} k^{7/6}\, H^{5/6} \sec^{11/6}\zeta \tag{4b}$$

$$\mu_{3u} = \text{Re} \int_0^H C_n^2(h)\left[\xi^{\frac{5}{6}}\left(i(1-\xi)\right)^{\frac{5}{6}}\right] dh \tag{4c}$$

$$\text{where } \xi = 1 - \frac{h}{H}$$

The scintillation statistics can be described with a log-normal distribution, where the variance equals the previously computed scintillation index σ_I^2. The power at the receive aperture fluctuates according to this log-normal distribution, as shown in Equation 5, where $p_I(I)$ represents the probability that the signal brightness equals to I and $\langle I \rangle$ is the average power received as computed in the link radiometry analysis. Figure 7 shows

the probability distributions for various values of scintillation indices. It can be seen that high scintillation index leads to high probability of fades and occasional surges in the received power.

$$p_I(I) = \frac{1}{\sqrt{2\pi}I\sigma_I}\exp\left\{-\frac{\left[\ln\left(\frac{I}{\langle I\rangle}\right)+\frac{1}{2}\sigma_I^2\right]^2}{2\sigma_I^2}\right\} \quad (5)$$
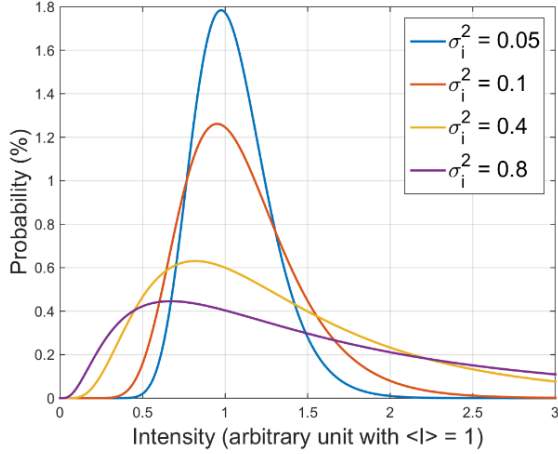

Figure 7 Probability distribution of the received power at various scintillation indices

Earth radiance model

While the other models in the simulation are concerned with the beacon signal received at the satellite terminal, beacon detection analysis also requires extensive knowledge of the background noise level during operation. To assess the background radiance level at 850 nm, data from the Landsat-8 mission was queried for multiple cloud coverage conditions at various cities in the United States during daytime. Landsat-8 is the most recent spacecraft in the Landsat series, a collaboration between NASA and US Geological Survey (USGS) with the goal of providing continuous global images in a number of spectral bands of scientific interests. The Landsat-8 spacecraft was launched in 2013 and is currently in a 705-km altitude circular polar orbit. The Landsat 8 spacecraft carries two sensors, the Operational Land Imager (OLI) and the Thermal Infrared Sensor (TIRS), collecting over 500 images per day. The OLI's spectral band consists of a NIR band (band 5) covering the range of 0.85 μm to 0.88 μm, coinciding with the selected beacon wavelength.[13] Since Landsat-8 level 1 data products are publicly available in the USGS archives with no restrictions, images in band 5 were queried and downloaded from the archive for further analysis. Examples of the images acquired from the database are shown in Figure 8 for the Boston region under four different cloud coverage conditions in the NIR band.
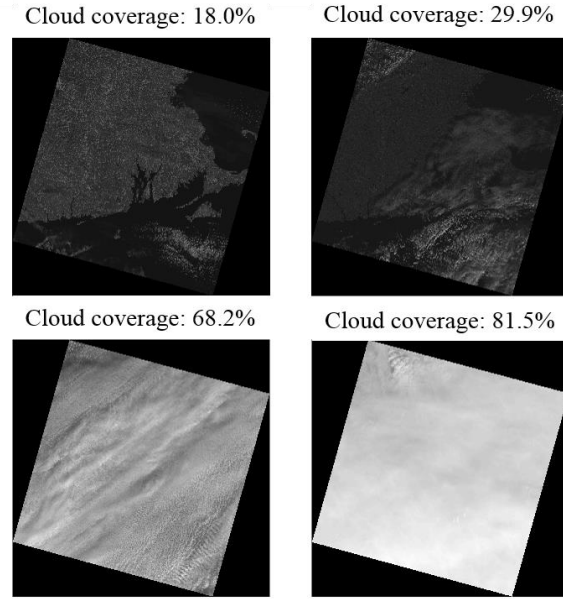
Figure 8 Landsat-8 OLI band 5 images of the Boston region under various cloud coverage conditions[14]

Each Landsat-8 OLI image downloaded is accompanied by a data file that contains radiometric calibration coefficients that can be used to convert image digital numbers (DN) to spectral radiance values of the scene at the sensor aperture. The calibration method is summarized in Equation 6.[15, 16]

$$L_\lambda = G_{rescale} \times Q_{cal} + B_{rescale} \quad (6)$$

where

L_λ	=	spectral radiance [W/(m² sr μm)]
Q_{cal}	=	quantized calibrated pixel value [DN]
$G_{rescale}$	=	band-specific rescaling gain factor [(W/(m² sr μm))/DN]
$B_{rescale}$	=	band-specific rescaling bias factor [W/(m² sr μm)]

Landsat 8 images in band 5 from Boston, Los Angeles, Seattle, and Houston were downloaded from the USGS server with 20 images per city for a variety of weather conditions during day time. The average brightness of each scene was first computed in DN, then converted to a corresponding average spectral radiance based on calibration coefficients and formula shown in Equation 6. The results were categorized by the level of cloud coverage, as shown in Figure 9.
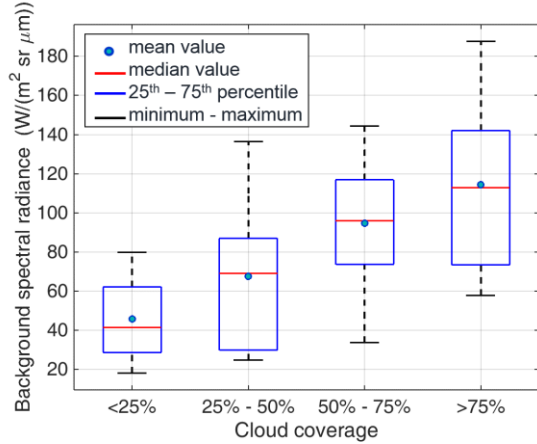
Figure 9 Background spectral radiance distributions in the spectral range of 0.85 µm – 0.88 µm under different cloud coverage conditions

The average spectral radiance for each cloud coverage condition were used as a baseline background noise in the beacon simulation and the maximum value in each case was used as the worst case scenarios, as summarized in Table 3. The highest spectral radiance in the >75% cloud coverage case is consistent with previous findings for background light in the NIR range under sunlit cloud conditions.[4, 9]

Table 3 Average and hightest spectral radiance values for various cloud coverage conditions

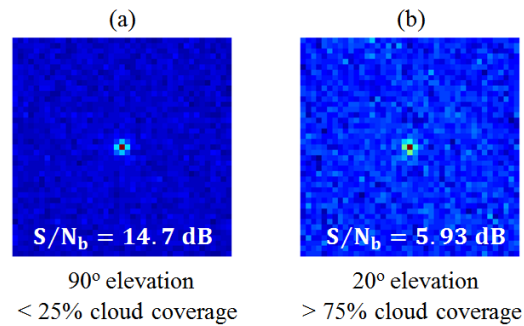| Cloud coverage	Spectral radiance [W/(m² sr µm)]	
	Average	Worst case
0% - 25%	45.9	79.9
25% - 50%	67.6	136.3
50% - 75%	94.7	144.3
75% - 100 %	114.5	187.7

Beacon image generation

After the model development process, simulated camera frames can be generated for various orbit configurations and weather conditions. The beacon frames are constructed by overlaying the image of the beacon's PSF on a background frame, with average brightness determined in the background radiance analysis. The average beacon brightness is determined in the link radiometry model, with intensity fluctuations following the atmospheric scintillation log-normal statistics, as described in the atmospheric turbulence model. The background frame was constructed pixel-by-pixel, where each pixel value follows a Poisson distribution with the mean value computed from the Earth radiance model. Detector's noise and signal's shot noise are also included in the frame generation process. The camera integration time is set such that the total number of electrons generated from both signal and noise sources reach 50% of detector's full-well capacity.

Since most of the beacon light will be concentrated in one pixel, false detection can occur if there exist background pixels brighter than the brightest beacon pixel. A figure of merit for beacon detection probability was defined as the ratio of the brightest beacon pixel over the brightest background pixel, referred to as the signal-to-brightest-noise level (S/N_b). The brightest beacon pixel can be found as the product of the signal photons from link radiometry analysis and the BPFF, as found in the camera model. The brightest background pixel can be estimated under the assumption that all pixels in the array are independent and follow a Poisson distribution with known mean value. An analytical estimation for S/N_b is shown in Equation 7, where S represents the signal level, $BPFF$ is the brightest pixel flux fraction, σ_n represents the standard deviation of all noise sources, and z is a parameter indicating the number standard deviations above the mean needed to find the brightest background pixel. The actual S/N_b value for each frame will vary due to the stochastic nature of the noise sources. Sample image frames under two different background light conditions and orbit configurations are shown in Figure 10, along with the corresponding S/N_b values. Figure 10 (a) shows the simulated beacon frame result for a 400-km altitude satellite at zenith with < 25% cloud coverage condition. Figure 10 (b) presents the result for the same satellite at 20° elevation with 75% - 100% cloud coverage, yielding a much lower S/N_b value than in the first case due to longer range and brighter background noise level.

$$S/N_b = \frac{S \times BPFF}{z\,\sigma_n} \quad (7)$$

$$\text{where } erf\left(\frac{z}{\sqrt{2}}\right) = 1 - \frac{1}{N_{pix}}$$

(a)   (b)

$S/N_b = 14.7\ dB$ $S/N_b = 5.93\ dB$

90° elevation   20° elevation
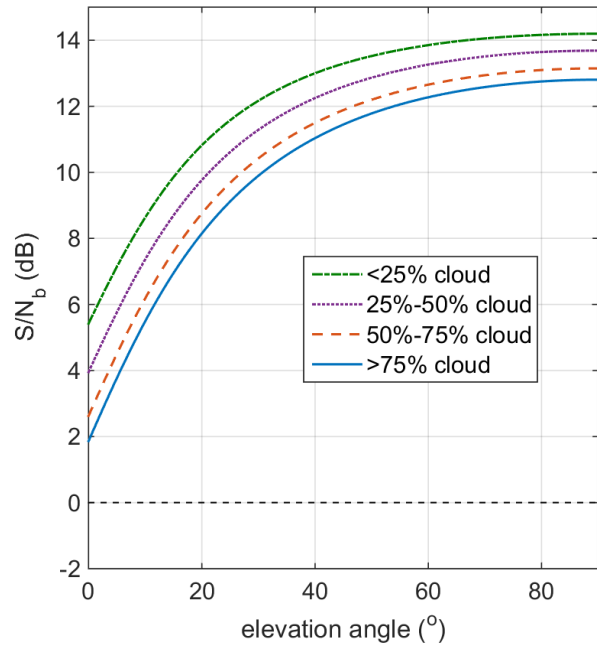
< 25% cloud coverage   > 75% cloud coverage

Figure 10 Simulated camera frames for a satellite at 400-km altitude with various elevation angles and background light conditions

SIMULATION RESULTS

The simulation inputs were constructed to represent the orbit configuration of a typical CubeSat in LEO in a circular 400-km altitude orbit. The laser transmitter power is fixed at 10 W with a beam divergence of 5 mrad, resulting in a power density below the maximum permissible exposure (MPE) limit as specified by the FAA[8]. The transmitter was assumed to include four independent laser sources, separated by the coherent length of the atmosphere at the ground station to mitigate the effect of scintillation. The simulation was run for multiple combinations of elevation angles and cloud coverage conditions to assess the applicability of the beacon camera design.

A preliminary analysis was done by computing an estimate of the average signal-to-brightest noise level S/N_b for each simulation input. Figure 11 shows the S/N_b curves for the four cloud conditions presented the sky brightness model over a full range of elevation angle. The spectral sky radiance values used are the average values presented in Table 3. It can be seen that all cloud conditions yield positive S/N_b values even at low elevation angles, giving a first-order validation for the feasibility of the approach. Since it has been shown in the atmospheric turbulence model that scintillation can cause deep fades in the signal power, the results in Figure 11 are not sufficient to realistically capture the full range of scenarios experienced by the beacon camera. The simulation was repeated with scintillation statistics included at each elevation angle to better represent the actual S/N_b distribution. Figure 12 shows the S/N_b curve for the >75% cloud coverage condition along with scintillation scattered points. The S/N_b value at each elevation angle was computed 20 times following a log-normal power distribution generated by the corresponding scintillation index. It can be seen that, as expected, the S/N_b performance is heavily degraded by scintillation, causing multiple data points to fade below the $S/N_b = 0$ threshold, indicating high probability of fading especially at low elevation angles.

In order to evaluate the performance of the beacon camera quantitatively, a Monte-Carlo beacon camera frame simulation was run with log-normal scintillation statistics, Poisson and Gaussian distributed noise sources, and a random-walk field angle inputs. Each camera frame is assumed to be independent since the time interval between each frame is much longer than the atmospheric and noise time scales. It is assumed that the location of the damaged pixels stays the same within each ground pass and only need to be removed once at the beginning of each pass. After dark frame subtraction to eliminate damaged pixels, each subsequent camera frame is subjected to a sequence of image processing steps, simulating actual flight software used to convert

**Figure 11 Average S/N_b for four cloud coverage conditions over a full range of elevation angle**
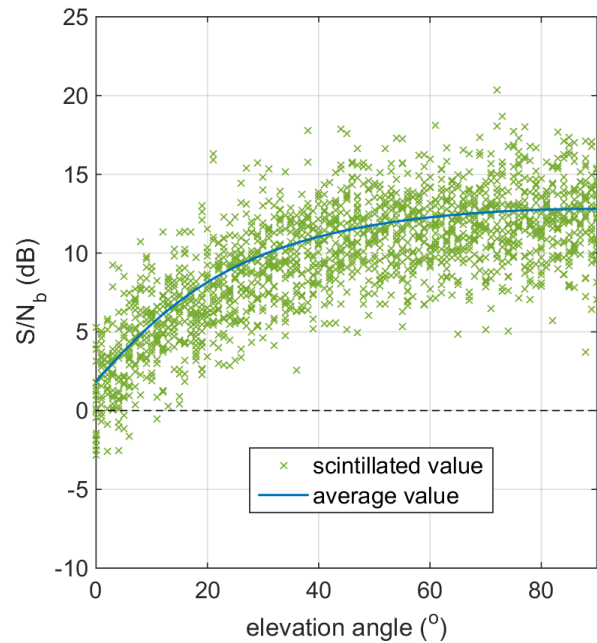
Figure 12 S/N_b fluctuations due to scintillation for all elevation angles under the >75% cloud coverage condition along with the average S/N_b curve

beacon image location to an attitude knowledge. The first step is to find the brightest pixel in the frame generated and identify a region-of-interest (ROI) around this bright pixel based on the expected size of the PSF. A threshold subtraction technique was implemented with

the threshold value computed as the average of a number of pixels outside of the ROI to reduce the background light in the cut-out image. Next, a center-of-mass centroid calculation is applied to all pixels within the ROI. The centroid error is computed by comparing this centroid value with the expected beam location based on the field angle input. This centroid error can be converted to a pointing error using properties of the imaging system. A fade instance occurs when a background pixel is brighter than the beacon signal, which can be identified by negative S/N_b values or sudden jumps in the beam centroid location. Figure 13 shows a time series of the simulated S/N_b values for the cloudy conditions at 20° elevation with a frame rate of 5 fps. It can be seen that the S/N_b value falls below zeros in 3 frames, indicating fading or false detection in 3 instances.
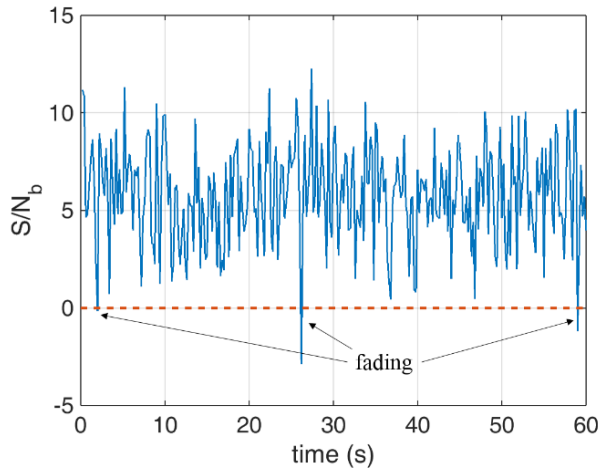
Figure 13 Simulated time series of the S/N_b values for the >75% cloud coverage condition at 20 deg elevation

For this Monte-Carlo simulation, the main scenarios to be tested are the maximum spectral radiance in the most cloud coverage case (187.7 W/m^2/sr/μm) and least cloud coverage case (79.9 W/m^2/sr/μm) at low elevation angles, representing an upper bound on the beacon tracking system attitude error for cloudy and clear-sky conditions. Figure 14 shows the fade probability results of the two cloud coverage conditions from 0° to 20° elevation angle with 5° increments. It can be seen that for both cloud coverage conditions, beacon detection can be done with high probability of success above 20° elevation angle, where the fade probability is less than 0.3% for the clear-sky condition and 1% for the bright reflective cloud condition.

The attitude knowledge results from the simulation are summarized in Figure 15. The attitude error are computed from the centroid error of the beacon image
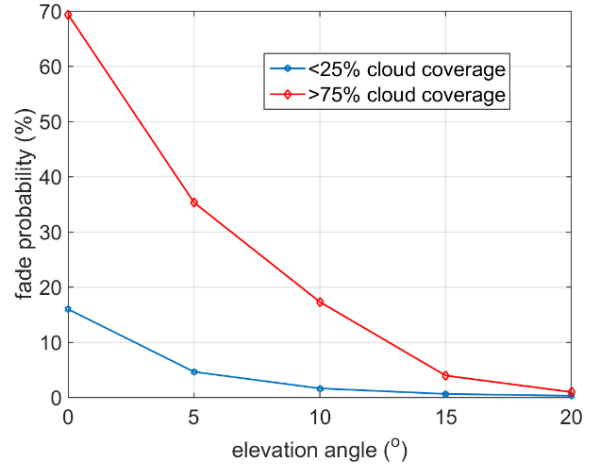
Figure 14 Fade probability for the <25% cloud coverage and >75% cloud coverage conditions at low elevation angles

when no fading occurs. It should be noted that the low variation in attitude accuracy in the cloudy case at low elevation angle is caused by a reduced number of valid data points due to fading. For both cloud coverage conditions at all elevation angles, the average attitude knowledge stays relatively constant at approximately 0.03 mrad, corresponding to approximately 0.5 pixel centroid error. It can be seen that when the beacon is detected, attitude knowledge remains well below 0.1 mrad even in extreme cloud reflectance conditions and low elevation angles.
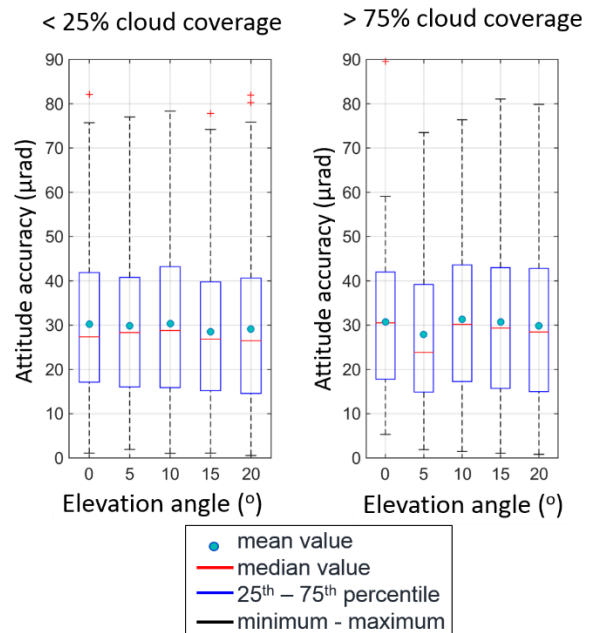
Figure 15 Attitude knowledge results for the < 25% and > 75% cloud coverage conditions at low elevation

CONCLUSION

This paper presents the design of a CubeSat-sized beacon camera that is capable of achieving sub-milliradian attitude knowledge relative to a ground target by using laser beacon detection techniques. The camera is a small, light module, with the size and weight corresponding to less than 0.1U. The system consists of only COTS components, leading to a cost-efficient design. A detailed simulation was constructed to assess the performance of the designed camera system, taking into consideration the laser beam radiometry, hardware model, atmospheric turbulence, and background sky radiance. Simulation results show that beacon detection can be done reliably above 20° elevation for most sky conditions, where the fade probability is less than 1%. When no fading occurs, the attitude accuracy has been shown to be consistently less than 0.1 mrad with an average attitude accuracy of 0.03 mrad. With this level of attitude accuracy, the laser beacon system presented has the potential to enable mission objectives that have not been previously demonstrated on CubeSat platforms, such as optical communication and precise ground target tracking.

Future work will focus on hardware characterization and testing under expected on-orbit conditions. For simulation validation, data from the OPALS mission has been requested and will be used to analyze atmospheric turbulence effects as well as expected on-orbit sky radiance. Finally, more work will be done in developing robust image processing techniques to improve the attitude accuracy of the system and reduce probability of false detection.

ACKNOWLEDGEMENT

REFERENCES

1. Palo, S. et al. (2013) "*An Agile Multi-use Nano Star Camera for Constellation Applications*". Proc. 27th Annual AIAA/USU Conference on Small Satellites.

2. Kahr, E., Montenbruck, O., and O'Keefe, K. (2013) "*Estimation and Analysis of Two-Line Elements for Small Satellites*", Journal of Spacecraft and Rockets, Vol. 50, No. 2, pp. 433-439.

3. Burnside, J. et al. (2011) "*Design of an Inertially Stabilized Telescope for the LLCD*". Proc. SPIE 7923, Free-Space Laser Communication Technologies XXIII, 79230L

4. Oaida, B. et al. (2013) "*OPALS: An Optical Communications Technology Demonstration from the International Space Station*". Aerospace Conference, 2013 IEEE

5. Janson, S. and Welle, R. (2013) "*The NASA Optical Communication and Sensor Demonstration Program*". Proc. 27th Annual AIAA/USU Conference on Small Satellites.

6. "*1/2.5-Inch 5Mp CMOS Digital Image Sensor*" Aptina Imaging MT9P031 Data Sheet rev G. https://www.aptina.com/products/image_sensors/mt9p031i12stc/

7. Nguyen, T. et al. (2015) "*Development of a pointing, acquisition, and tracking system for a CubeSat optical communication module*" Proc. SPIE 9354, Free-Space Laser Communication and Atmospheric Propagation XXVII, 93540O.

8. (2004) "*Outdoor Laser Operations, Advisory Circular*". U.S. Department of Transportation. Federal Aviation Administration. 12/30/2004. http://www.faa.gov/documentLibrary/media/Advisory_Circular/AC70-1.pdf

9. Lambert, S. and Casey, W. (1995) "*Laser Communications in Space*". Artech House, Inc. Norwood, MA, 1995. ISBN-13: 978-0890067222

10. Strohbehn, J. (1978) "*Laser Beam Propagation in the Atmosphere*". Springer-Varlag Berlin Heidelberg, NY, 1978. ISBN: 978-3-540-08812-7

11. Andrews, L. et al. (2005) "*Laser Beam Propagation through Random Media, Second Edition*" (SPIE Press Monograph Vol. PM152). SPIE – The International Society for Optical Engineering. ISBN-13: 978-0819459480

12. Hemmati, H. (2009) "*Near-Earth Laser Communications (Optical Science and Engineering)*". CRC Press. 2009. ISBN-13: 978-0824753818.

13. Roy, D. et al. (2014). "*Landsat-8: Science and Product Vision for Terrestrial Global Change Research*" Remote Sensing of Environment, Volume 145, p. 154-172

14. US Geological Survey (USGS) Earth Resources Observation and Science (EROS) LandSat 8 OLI/TIRS data base. http://earthexplorer.usgs.gov

15. Chander, G. (2009) "*Summary of current radiometric calibration for LandSat MSS, TM, ETM+, and EO-1 ALI sensors*." Remote Sensing of Environment 113.

16. "*LandSat 7 Science Data Users Handbook*", NASA's Goddard Space Flight Center in Greenbelt, Maryland. http://landsathandbook.gsfc.nasa.gov/pdfs/Landsat7_Handbook.pdf